



Cellular migration into a subretinal honeycomb-shaped prosthesis for high-resolution prosthetic vision

Mohajeet B. Bhuckory^{a,b,1,2} , Bing-Yi Wang^{a,c,1} , Zhijie Charles Chen^{a,d}, Andrew Shin^e, Tiffany Huang^d , Ludwig Galambos^a, Efstathios Vounotrypidis^b, Keith Mathieson^f , Theodore Kamins^d , and Daniel Palanker^{a,b}

Edited by Serge Picaud, Institut de la vision, Paris, France; received May 3, 2023; accepted September 8, 2023 by Editorial Board Member Jeremy Nathans

In patients blinded by geographic atrophy, a subretinal photovoltaic implant with 100 μm pixels provided visual acuity closely matching the pixel pitch. However, such flat bipolar pixels cannot be scaled below 75 μm, limiting the attainable visual acuity. This limitation can be overcome by shaping the electric field with 3-dimensional (3-D) electrodes. In particular, elevating the return electrode on top of the honeycomb-shaped vertical walls surrounding each pixel extends the electric field vertically and decouples its penetration into tissue from the pixel width. This approach relies on migration of the retinal cells into the honeycomb wells. Here, we demonstrate that majority of the inner retinal neurons migrate into the 25 μm deep wells, leaving the third-order neurons, such as amacrine and ganglion cells, outside. This enables selective stimulation of the second-order neurons inside the wells, thus preserving the intraretinal signal processing in prosthetic vision. Comparable glial response to that with flat implants suggests that migration and separation of the retinal cells by the walls does not cause additional stress. Furthermore, retinal migration into the honeycombs does not negatively affect its electrical excitability, while grating acuity matches the pixel pitch down to 40 μm and reaches the 27 μm limit of natural resolution in rats with 20 μm pixels. These findings pave the way for 3-D subretinal prostheses with pixel sizes of cellular dimensions.

retinal prosthesis | vision restoration | neuronal migration | age-related macular degeneration | blindness

Retinal degenerative diseases, such as age-related macular degeneration (AMD) and retinitis pigmentosa, are among the leading causes of untreatable visual impairment. Despite the different pathophysiology, both diseases ultimately lead to loss of the photoreceptors, while leaving the inner retinal neurons relatively intact (1–3), albeit with some rewiring (4, 5). Electrical stimulation of the remaining inner retinal neurons can elicit visual percepts, thereby enabling restoration of sight (6–8).

We developed an optoelectronic substitute for the lost photoreceptors: a wireless photovoltaic subretinal implant activated by light (9, 10). Images of the visual scenes captured by a video camera are processed and projected by augmented-reality glasses onto a subretinal photodiode array using intense pulsed light. Photovoltaic pixels in the array convert this light into biphasic pulses of electric current, which stimulate the second-order neurons in the inner nuclear layer (INL)—primarily the bipolar cells (BC). To avoid perception of this light by the remaining photoreceptors in the peripheral region, we use a near-infrared (NIR, 880 nm) wavelength.

This approach offers multiple advantages: 1) thousands of pixels in the implant can be activated simultaneously and independently; 2) a lack of wires enables reliable encapsulation of the implant and greatly simplifies the surgical procedure; 3) besides autofocusing, an external camera allows operation over a wide range of ambient illumination and provides adjustable image processing optimized for the dynamic range of the implant; 4) light-sensitive pixels maintain the natural link between eye movements and image perception; 5) network-mediated retinal stimulation retains many features of the natural signal processing, including antagonistic center-surround (11), flicker fusion at high frequencies, and nonlinear summation of the RGC (ganglion cell) subunits (9), amongst others.

This approach has been employed clinically, where PRIMA implants (Pixium Vision SA, Paris, France) with 100 μm pixels, were implanted in AMD patients. These patients perceived monochromatic formed vision in the previous scotomata, with a prosthetic visual acuity closely matching the pixel size: 1.17 ± 0.13 pixels, corresponding to the Snellen range of 20/438 to 20/550 (100 μm pixel corresponds to 20/420 acuity) (12, 13). Even more remarkable is that the prosthetic central vision in AMD patients is perceived simultaneously with the remaining natural peripheral vision (13).

Significance

The most promising results in restoration of sight to patients blinded by age-related macular degeneration (AMD) to date have been achieved by replacing the missing photoreceptors with photovoltaic pixels. Prosthetic visual acuity in AMD patients closely matches the sampling limit of the 100 μm pixel size, but further miniaturizing flat bipolar pixels is challenging. We demonstrate the feasibility of reducing pixel size down to 20 μm using a 3-dimensional honeycomb-shaped interface with the retina, allowing retinal neurons to migrate into wells containing the electrodes, thereby getting exposed to a strong electric field, independent of pixel size. Our results demonstrate good compatibility of such implants with the retina and high resolution, which opens the door to highly functional restoration of sight.

Author contributions: M.B.B., K.M., T.K., and D.P. designed research; M.B.B., B.-Y.W., Z.C.C., A.S., T.H., L.G., and E.V. performed research; M.B.B., B.-Y.W., Z.C.C., and D.P. analyzed data; and M.B.B., B.-Y.W., Z.C.C., A.S., K.M., T.K., and D.P. wrote the paper.

Competing interest statement: T.K.: consultant (Pixium Vision); D.P.: patent and consultant (Pixium Vision). The other authors declare no competing interests.

This article is a PNAS Direct Submission. S.P. is a guest editor invited by the Editorial Board.

Copyright © 2023 the Author(s). Published by PNAS. This article is distributed under Creative Commons Attribution-NonCommercial-NoDerivatives License 4.0 (CC BY-NC-ND).

¹M.B.B. and B.-Y.W. contributed equally to this work.

²To whom correspondence may be addressed. Email: bhuckory@stanford.edu.

This article contains supporting information online at <https://www.pnas.org/lookup/suppl/doi:10.1073/pnas.2307380120/-DCSupplemental>.

Published October 13, 2023.

However, for a wider adoption of this approach by AMD patients, prosthetic acuity should significantly exceed that of their remaining peripheral vision, which is typically no worse than 20/400. The Nyquist sampling limit for an acuity of 20/200 corresponds to 50 μm pixels, and 20/100 to 25 μm . As with natural vision, prosthetic acuity is limited not only by the spatial resolution of the stimulation patterns (i.e., pixel size and the field spread) but also by their contrast, which is affected by crosstalk between the neighboring electrodes (14). Lateral spread of electric field can be confined by the local return electrodes in each pixel, as in the PRIMA implant (Fig. 1A), but scaling down such pixels is difficult because the penetration depth of electric field in tissue is constrained by the distance between the active and return electrodes, which is about half

of the pixel radius (15). As a result, the stimulation threshold in such geometry rapidly increases with a decreasing pixel size and exceeds the safe charge injection limit for pixels below 75 μm in human retina (16) and 55 μm in rats (17), even with one of the best electrode materials—sputtered iridium oxide films (SIROF) (15).

To overcome this limitation, we proposed a 3-dimensional (3-D) “honeycomb” configuration of the implant, with the active electrodes at the bottom and return electrodes at the top of vertical walls (15, 18) (Fig. 1B). In this configuration, the electric field in the cavities is oriented nearly vertically, parallel to the direction of the BCs, thereby reducing the stimulation threshold. Decoupling the electric field penetration depth (defined by the cavity height) from the pixel width enables scaling the pixel size down to cellular

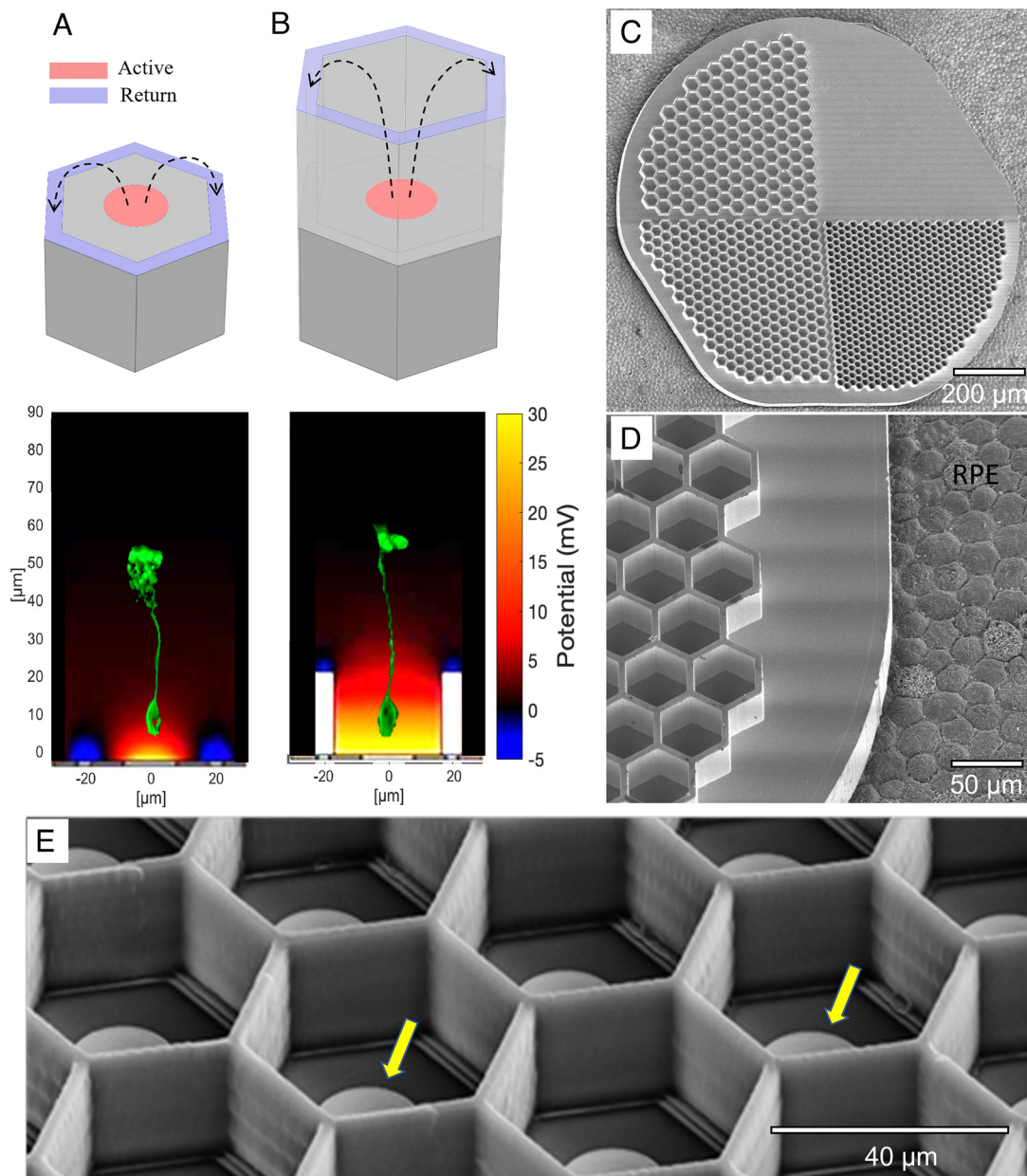


Fig. 1. Subretinal implants of flat and 3-D geometries. (A) A flat bipolar pixel containing the central active (red) and a circumferential return electrode (blue). (B) A honeycomb-shaped pixel with the return electrode (blue) elevated on 25- μm -tall walls. Bottom panels in A and B show the corresponding simulated electric fields (current = 68 nA) and immunolabelled BCs (Protein kinase C alpha; PKC α , green) illustrating their position and size with respect to the field penetration. (C) Scanning electron microscopy of passive honeycomb array with 4 quadrants: flat, 20-, 30-, and 40- μm wells. (D) Higher magnification of the 40- μm wells imaged on porcine RPE for size illustration. (E) Active 40- μm pixels with polymer honeycomb walls. Yellow arrows indicate the electrodes.

dimensions. Furthermore, confinement of the electric field within cavities limits the cross talk from neighboring pixels.

The honeycomb approach is based on retinal migration: Within days after the implantation, inner retinal neurons migrate into open spaces in a subretinal implant (19–21). For the network-mediated retinal stimulation, the second-order neurons should be activated below the threshold of the direct stimulation of the third-order retinal neurons. Therefore, the wall height must accommodate the BCs within the cavities, while leaving the amacrine (AC) and RGCs outside.

Here, we present a detailed anatomical characterization of the retinal migration in Royal College Surgeon (RCS) rats after subretinal implantation of the honeycomb arrays with 20, 30, and 40- μm pixels. By recording the visually evoked potential (VEP), we assessed the effect of this migration on retinal excitability and measured the spatial resolution of the retinal stimulation using alternating gratings. Our results suggest that retinal prostheses with such 3-D structures enable the retinal stimulation with pixels down to 20 μm in size, geometrically corresponding to a visual acuity of 20/80, which would significantly help many patients impaired by atrophic AMD.

Results

INL Neurons. To assess the migration of the target BCs and other inner retinal cells into honeycomb wells, 1-mm silicon devices (Fig. 1 C and D) were implanted into the subretinal space of RCS rats (6 to 9 mo old, $n = 33$) for 6 wk. Each device comprised four quadrants (Fig. 1C): flat, 20, 30, and 40 μm honeycombs to assess the effect of pixel size on retinal integration. The 25- μm height of the walls was chosen to accommodate the migration of second-order neurons (primarily BCs) and exclude the third-order neurons (ACs and RGCs) from the wells. Characterization of cellular integration with the implants was performed on reconstructed confocal acquisitions of the whole-mounted retina-honeycomb-sclera complex. Overview of the implant from the top of the honeycomb to the base of the well reveals a uniform fill by rod and cone bipolar immuno-labeled cells along with other nonlabeled DAPI nuclei throughout the wells of different sizes (Fig. 2 A, C, and E). Cross-sectional (side) views through a randomly selected honeycomb row, projected from the middle of the wells to the sidewall, show migration to the base of the implants, while some BCs remain above the honeycomb walls. The fraction of the rod

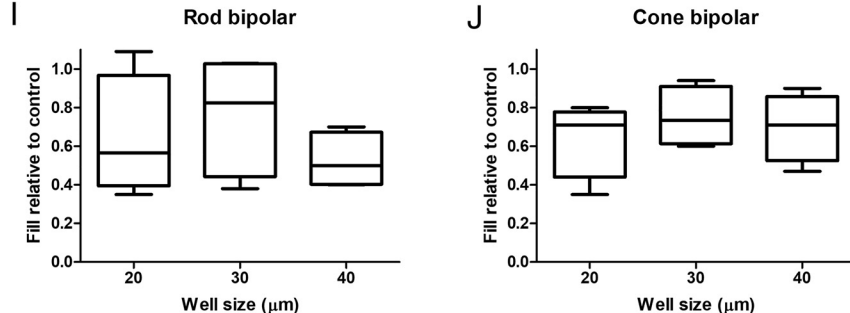
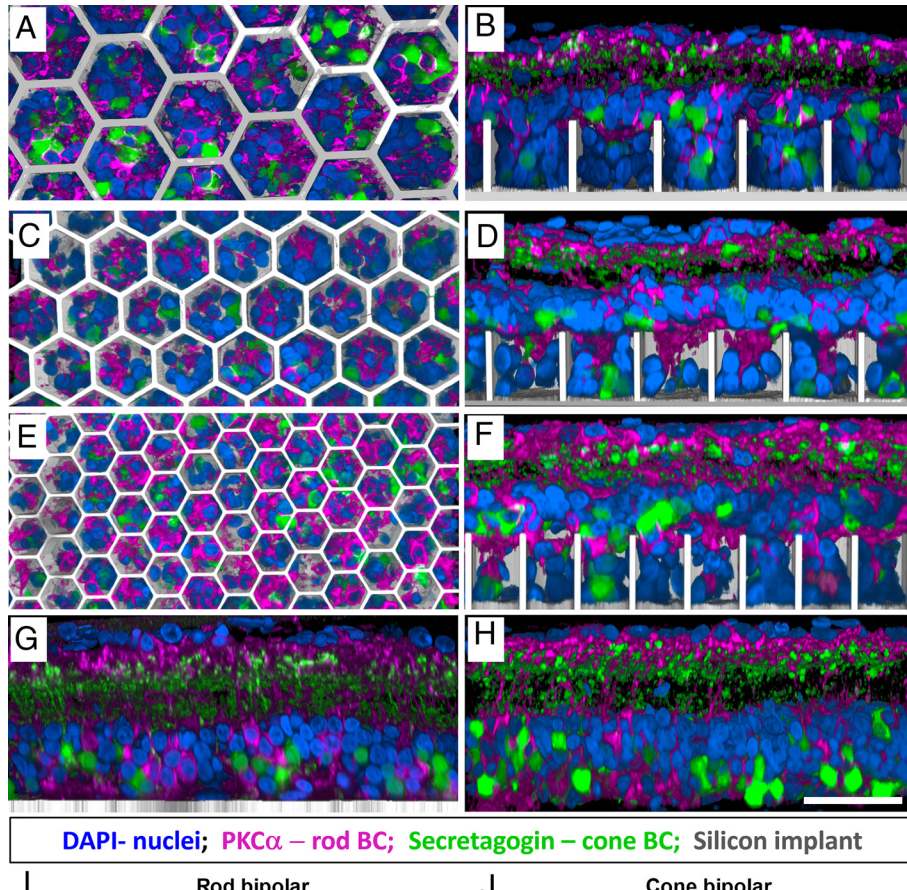


Fig. 2. Confocal images of immuno-labelled rod (PKC α : magenta) and cone (secretagogin: green) BCs. Top-down and side-view of the retina above and inside the honeycomb wells of 40 (A and B), 30 (C and D), and 20 (E and F) μm . DAPI (blue) labels the nuclei, and the implant is shown in gray. (Scale bar is 50 μm .) BCs maintain their structural integrity comparable to that with a flat implant (G) and a nonimplanted RCS rat retina (H). Fraction of migrated rod (I) and cone (J) BCs within the wells of 20, 30, and 40 μm , relative to nonimplanted retina. Boxes extend from 25th to 75th percentile from the median line and the whiskers—from smallest to largest value.

BCs, relative to its average number in the nonimplanted control, inside the 25 μm tall walls of 20, 30 and 40 μm honeycombs was 0.64 ± 0.31 , 0.77 ± 0.31 , and 0.53 ± 0.14 , respectively (Fig. 2*J*). For cone BCs these fractions were 0.64 ± 0.19 , 0.75 ± 0.15 , and 0.70 ± 0.17 , respectively (Fig. 2*J*). Both BC types maintain their structural integrity, with unchanged stratification in the IPL.

The other type of second-order neurons, horizontal cells, undergo dendritic and axonal degeneration but remain in similar numbers after photoreceptor degeneration in RCS retina, compared to healthy retina (22). Horizontal cells and their axons were observed close to the subretinal space in the nonimplanted control (Fig. 3*H*) and interfacing with the flat implant control (Fig. 3*G*). In the presence of the 3-D implants, most horizontal cells migrated into the honeycombs: 0.85 ± 0.09 , 0.70 ± 0.22 , and 0.87 ± 0.17 in 20-, 30-, and 40- μm wells, respectively (Fig. 3*I*). However, after migration, the horizontal cells are now in the middle of the INL, close to the top of the wells (Fig. 3 *B*, *D*, and *F*). The top-down view shows cell bodies inside the wells, while their axons remain above the honeycomb walls (Fig. 3 *A*, *C*, and *E*; yellow arrows), as opposed to the natural morphology with their axons below the cell bodies (Fig. 3*H*).

The third-order neurons of the INL, AC, play a major role in signal transduction and modulation between bipolar and RGCs

(23). Therefore, direct electrical stimulation of the ACs could lead to alteration of the natural signal processing. None of the immunolabeled subset of cholinergic starburst ACs were observed inside the wells in the top-down view (Fig. 4 *A*, *C*, and *E*). AC somas remain above the walls of all honeycomb sizes (Fig. 4 *B*, *D*, and *F*) away from the electric field, and preserve a similar IPL stratification as in the nonimplanted control (Fig. 4*H*).

Inner Retinal Vasculature. An important consideration when dealing with retinal prosthesis is whether the device will allow normal oxygenation of migrated cells. Subretinal implants create a barrier between the choroidal supply and the retina. However, since the implants are inserted after a compete degeneration of photoreceptors, the choroidal supply is not necessary as the inner retina has its own vasculature. The inner retinal vasculature is grouped into the superficial vascular complexes (NFL to IPL) and the deep vascular complexes (DVC; IPL to OPL) (24). The deep capillary plexus (DCP) of DVC comprises of vessels in the INL and OPL (subretinal space in degenerated RCS retina) as seen in Fig. 5*G*.

The presence of a flat subretinal implant does not affect the DCP density or location, as compared to nonimplanted area

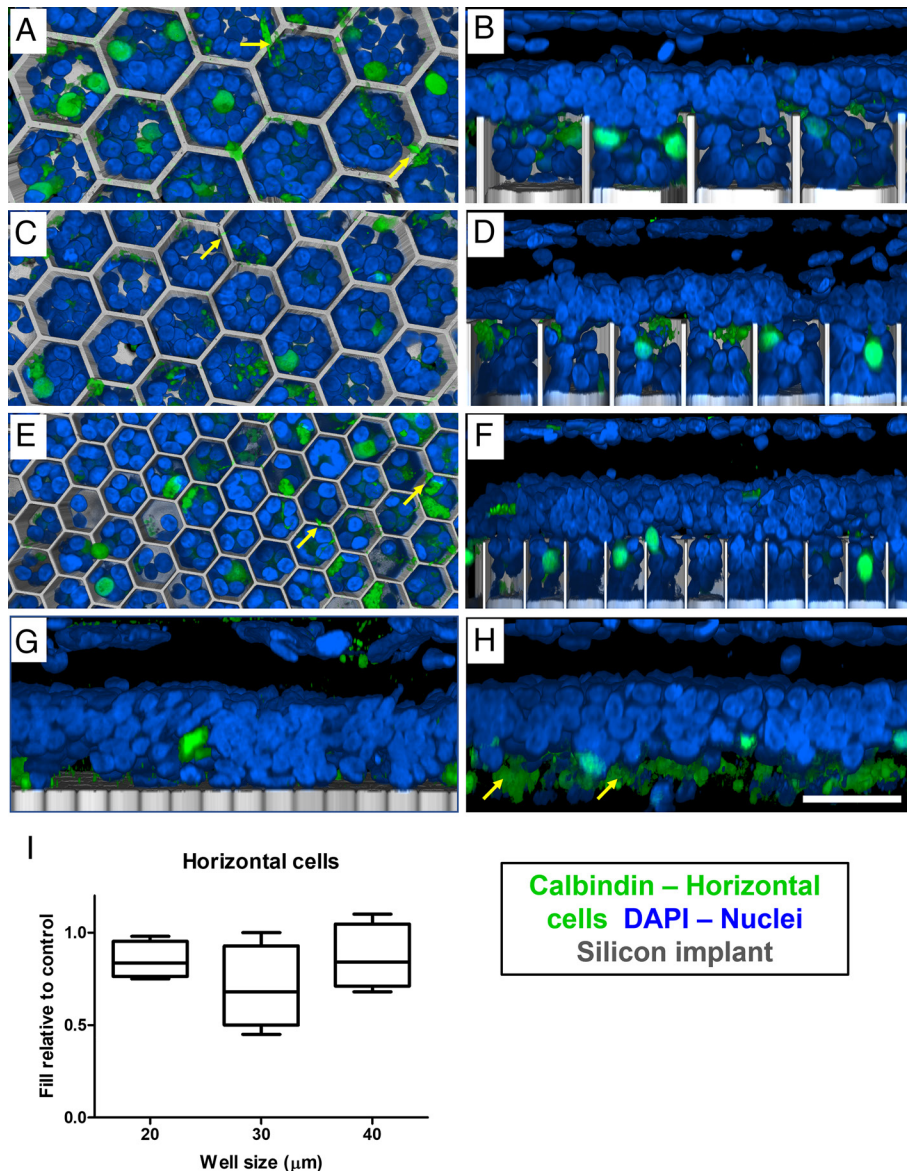
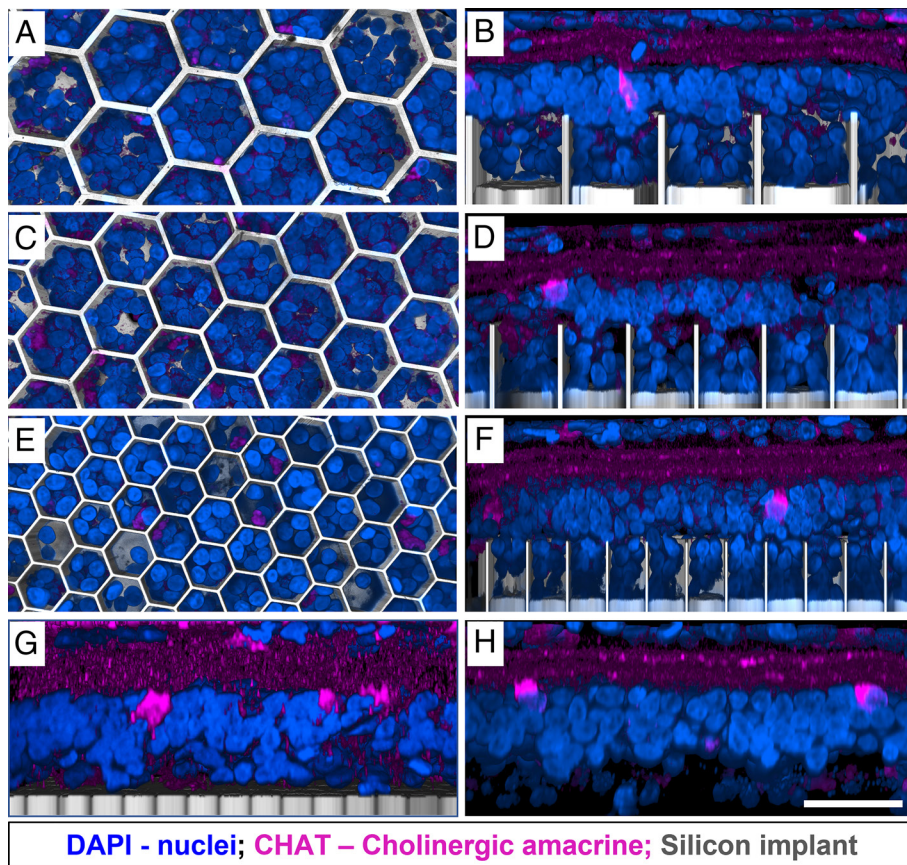


Fig. 3. Confocal images of horizontal cells immuno-labelled with calbindin (green). DAPI (blue) label all other nuclei, and the implant is shown in gray. (Scale bar is 50 μm .) Top-down view (left column) and side view (right column) of the retina above and inside honeycomb wells of 40 (*A* and *B*), 30 (*C* and *D*), and 20 (*E* and *F*) μm . In the flat implant control (*G*) and nonimplanted control (*H*), the cell bodies are above the axons (yellow arrows). In contrast, horizontal cells bodies migrate into wells, but their axons and dendrites (yellow arrows in *A*, *C*, and *E*) remain above the walls. (*I*) Box extends from 25th to 75th percentile from the median line and whiskers—from smallest to largest value.



DAPI - nuclei; CHAT – Cholinergic amacrine; Silicon implant

Fig. 4. ACs immuno-labelled with choline acetyltransferase (CHAT: magenta). DAPI (blue) label the nuclei, and the implant is shown in gray. (Scale bar is 50 μm .) Top-down view (left column) and side view (right column) show the retina above and inside the honeycomb wells of 40 (*A* and *B*), 30 (*C* and *D*), and 20 (*E* and *F*) μm . ACs remain above the walls for all honeycomb sizes and retain their IPL stratification and cell body position in the INL, similar to the flat implant control (*G*) and nonimplanted control (*H*).

(Fig. 5*H*). With a 3-D device, the DCP vessels rest on top of the walls (Fig. 5 *B*, *D*, and *F*) and do not migrate into the wells of any size studied. Nuclei (likely second-order neurons observed in Figs. 2 and 3) migrate past the vessels into the wells (Fig. 5 *A*, *C*, and *E*) and retain a healthy appearance 6 to 9 wk after implantation, suggesting proper oxygenation and nutrients supply.

Retinal Glial Response. Müller glia span the entire thickness of the retina and ensheathe all its neurons. Müller cells were immunolabelled by its cytoplasmic enzyme glutamine synthetase (GS), and Müller cell nuclei—by its transcription factor, SOX9. Migration of the Müller cell nuclei is known to happen after the retinal damage (25), similar to subretinal surgery for implantation of flat and 3-D arrays. In the nonimplanted control, Müller cell nuclei are arranged orderly in the middle of the INL (Fig. 6*H*). After retinal integration with the honeycombs, some of the Müller cell processes and nuclei can be observed inside the wells in the top-down view (Fig. 6 *A*, *C*, and *E*). Most of the Müller nuclei migrate into the 30- μm and 40- μm wells: 0.73 ± 0.06 and 0.70 ± 0.08 , respectively, but only 0.36 ± 0.12 into 20- μm wells (Fig. 6*I*) relative to the nonimplanted control. The side views show some Müller cell bodies even reaching the bottom of the larger wells but very shallow penetration into the 20- μm wells (Fig. 6 *B*, *D*, and *F*).

Another consequence of a retinal insult is the Müller cell activation, which may lead to glial scar formation (25). On a flat implant, glial scars may increase the distance and impedance between the active electrodes and the BCs. This may be even more problematic with honeycomb implants as scar tissue could prevent migration of the BCs into the wells and result in poor retinal stimulation. Müller cell activation was assessed by immunostaining the tissues with Glial Fibrillary Acidic Protein (GFAP), which

is up-regulated in Müller cells (26, 27) and astrocytes (Fig. 7). GFAP activation and clusters (indicative of a glial scar; yellow arrows) can be observed in the INL of the nonimplanted RCS retina and flat implant control (Fig. 7 *G* and *H*). Migration of the Müller cells into the wells increased with the size of the honeycombs: 0.43 ± 0.07 , 0.60 ± 0.03 , and 0.71 ± 0.12 into 20 μm , 30 μm , and 40- μm wells, relative to the position of GFAP staining in the INL in nonimplanted controls. In contrast, the average penetration depth of all nuclei (DAPI staining in Fig. 7*J*) does not exhibit the well-width selectivity: 0.97 ± 0.08 , 1.00 ± 0.11 , 1.02 ± 0.06 of all INL nuclei, relative to the nonimplanted control, migrate into 20- μm , 30- μm , and 40- μm pixels, respectively.

Migration of neurons (Figs. 2 and 3) and all nuclei (Fig. 7*J*) deeper than Müller cell nucleus into the wells (specially in 20- μm wells) indicate that even in the event of glial scar formation (GFAP clusters and penetration in Fig. 7*J*), migration of the retinal neurons into honeycombs is not impeded.

Retinal Stimulation Post Migration. To assess whether the electrical excitability of the retina was affected by migration into the honeycombs, polymer-based nonconducting vertical walls were formed on flat arrays with photovoltaic pixels, having a common return electrode only near the periphery of the array (monopolar configuration; Fig. 1*E*) (28). Electric field in such wells is oriented vertically, similarly to that expected with an elevated return electrode on top of conductive walls. Such arrays were implanted into the subretinal space of RCS rats, temporal-dorsal to the optic nerve head (Fig. 8*A*). Surgical success was assessed using OCT (OpticalCoherence Tomography) immediately after the surgery, and migration was assessed 6 wk after implantation. After surgery, the retina was separated from the implant by a thin layer of debris

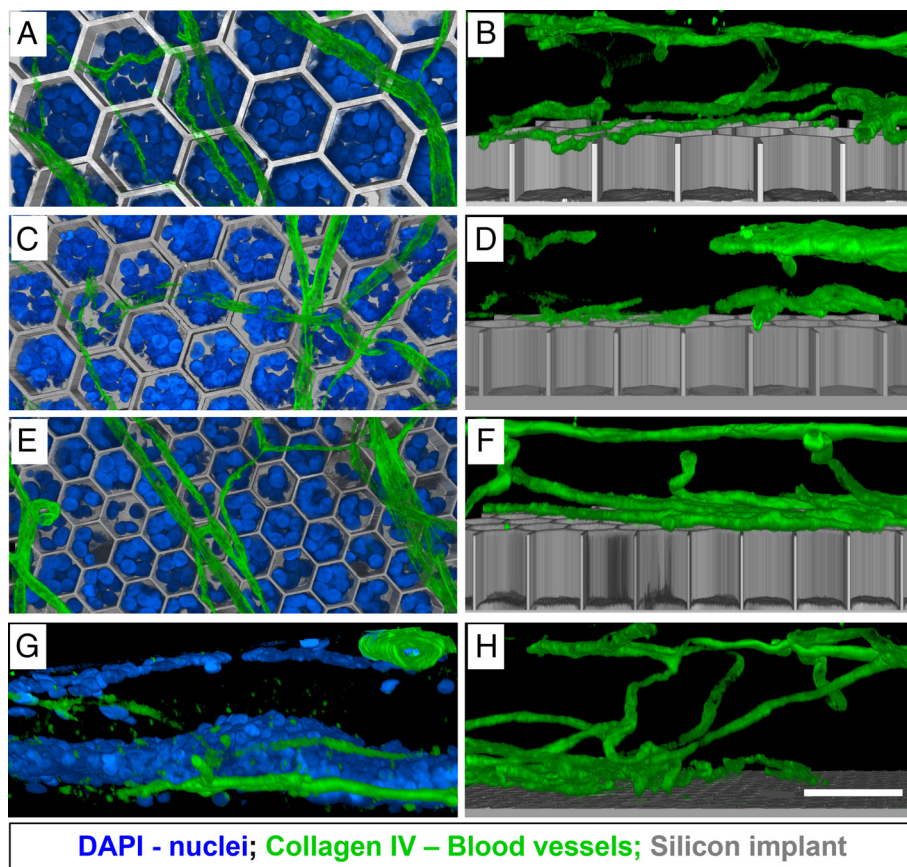


Fig. 5. Retinal blood vessels immuno-labelled with collagen IV (green). DAPI (blue) label the nuclei, and the implant is shown in gray. (Scale bar is 50 μm .) Top-down view (left column) and side view (right column) show the vasculature above the honeycomb wells of 40 (*A* and *B*), 30 (*C* and *D*), and 20 (*E* and *F*) μm , while the retinal cells migrated around the vessels into the wells (*A*, *C*, and *E*). The DCP interface with the subretinal space in a control retina (*G*) and with a flat implant (*H*).

and fluid (Fig. 8 *B* and *D*). Six weeks after implantation, the INL is barely detectable by OCT above the honeycombs (Fig. 8 *C* and *E*) but visible outside the implant, indicating the INL migration into the wells.

VEPs were recorded via transcranial electrodes above the visual cortices, with NIR stimuli at 2 Hz, pulse duration of 10 ms, and peak irradiance ranging from 0.002 to 4.7 mW/mm² on the retina. The VEP was assessed with monopolar flat devices having 20 μm and 40- μm pixels and with 3-D printed walls on similar pixels for comparison (*SI Appendix*, Fig. S1). Stimulation thresholds with the 3D devices (0.064 ± 0.034 mW/mm²) closely matched that of full-field stimulation with the flat implants (0.057 ± 0.029 mW/mm²), where neighboring pixels combine to align the E-field vertically. This suggests that not only is the number of BCs preserved post migration (Fig. 2) but also is the electrical excitability of the retina. It is important to note that simultaneous activation of all the pixels in a monopolar array results in summation of their electric fields, adding up to a field similar to that of a single large electrode, equal in size to the whole array. Within the thickness of inner retina (<0.1 mm), this field is nearly vertical, similar to the vertical field inside 3-D cavities. However, when single flat pixels (or sparse patterns) are activated, their electric field is much more divergent and shallower, and hence inferior to nearly vertical field inside 3-D cavities.

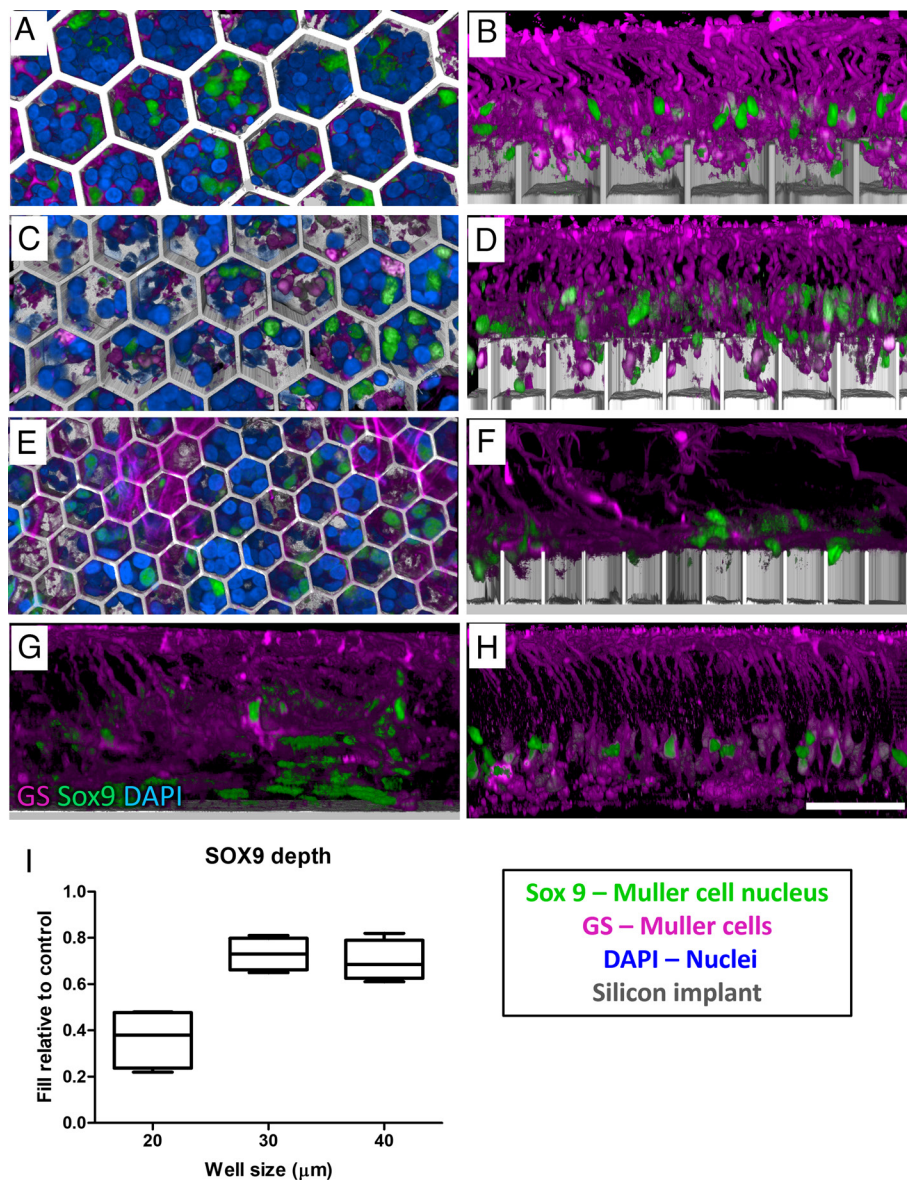
To assess the spatial resolution of prosthetic vision with honeycomb implants, we measured grating acuity after the cell migration is complete (>8 wk). *SI Appendix*, Fig. S2 demonstrates the typical VEP traces in response to alternating grating of various stripe widths, in rats with 40- μm and 20- μm honeycombs, respectively. As shown in Fig. 8*F*, the fitting line crosses the noise level at 34.5 ± 4.8 μm , matching the pixel pitch of 40- μm hexagonal array (40

$\cos 30^\circ = 34.6$). As shown in Fig. 8*G*, with 20- μm arrays, the measured acuity limit was much larger than the 17- μm pixel pitch: 26.0 ± 3.8 μm . Taking into account that in a rat eye, 1 degree of the visual angle corresponds to 65 mm on the retina (29), grating with 26 mm stripe width corresponds to 1.2 cycle per degree, matching the limit of natural visual acuity in rats (30–32).

Discussion

Recent clinical trials with flat photovoltaic implants having 100- μm pixels (PRIMA, Pixium Vision SA, Paris, France) demonstrated restoration of central vision in AMD patients with acuity up to 20/438 (12, 13). To further improve prosthetic visual acuity, pixel size should be decreased, while retaining sufficiently deep penetration of electric field into the INL, which is impossible with the flat bipolar pixel design (16). 3-D subretinal implants can address this limitation by decoupling the field penetration depth from the pixel width, thereby enabling smaller pixels. The elevated return electrode also aligns the electric field along the BCs, decreasing the stimulation threshold, reducing the cross talk between neighboring pixels and providing better contrast (15). In this study, we focus on the key aspects that the success of this technology is contingent upon, namely a) migration of BCs into the wells while retaining their electrical excitability, b) sufficient oxygenation and nutrient delivery inside the wells, c) minimal glial reactivity, and d) the wall height minimizing direct stimulation of the third-order neurons.

Retinal cell migration is a well-characterized phenomenon during ocular development (31–36). Bidirectional movement of the newborn neurons is essential to stratification of the retinal tissue. In the degenerate retina, some level of migration also exists as part



of the retinal remodeling process (4, 37–42); retinal response to laser damage of photoreceptors includes migration of the cone photoreceptors into the damage zone (43), BCs rewiring to photoreceptors outside the damage zone (41), migration of the Müller cells nuclei (30, 38, 41, 44), and displacement of tertiary neurons (45). Rapid and large-scale migration has been observed even ex vivo, when a perforated membrane was placed on the photoreceptor side of the retina, while no migration was observed when such membrane was placed on the epiretinal side (20). Similarly, rapid migration through a perforated subretinal membrane was observed with a degenerate retina in vivo (20).

In this study, the presence of the 3-D honeycomb implants induced a “de nouveau remodeling phase”, with migration of several cell types into the wells. BCs constituted the majority of migrated cells inside the honeycombs of all sizes, exceeding the estimated 8% of BCs required for eliciting the VEP response (15). While 40- and 30- μ m-wide honeycombs provided better cellular migration, the number of BC in 20- μ m wells should be sufficient for eliciting VEP, and this smaller pixel size may enable higher acuity in human patients. The presence of the horizontal cells in

the wells is unlikely to affect the retinal response since their normal synaptic connections with photoreceptors are missing, although random synaptic rewiring of horizontal cells in the degenerate retina (37, 39) cannot be excluded.

The optimal height of honeycomb walls is critical in allowing significant amount of the second-order neurons to migrate into the wells while providing sufficient oxygenation and excluding the third-order neurons. While blood vessels inside the wells may provide better oxygenation, the DCP are not numerous enough to migrate into every well within an implant (19). Furthermore, bending the laterally spanning vessels into cavities may induce damage to the vessel walls and compromise the retinal blood barrier. With 25- μ m-high walls, the DCP and ACs remain above the honeycomb walls while other INL cells migrate into the wells. The overall number of the cells in the INL is comparable to the controls, the cells retain a healthy morphology and more importantly, the retina remains electrically excitable, suggesting that proper diffusion of oxygen and nutrients is maintained over the induced 25- μ m-deep separation. ACs did not migrate into the wells and maintained their OPL stratification, contrary to the

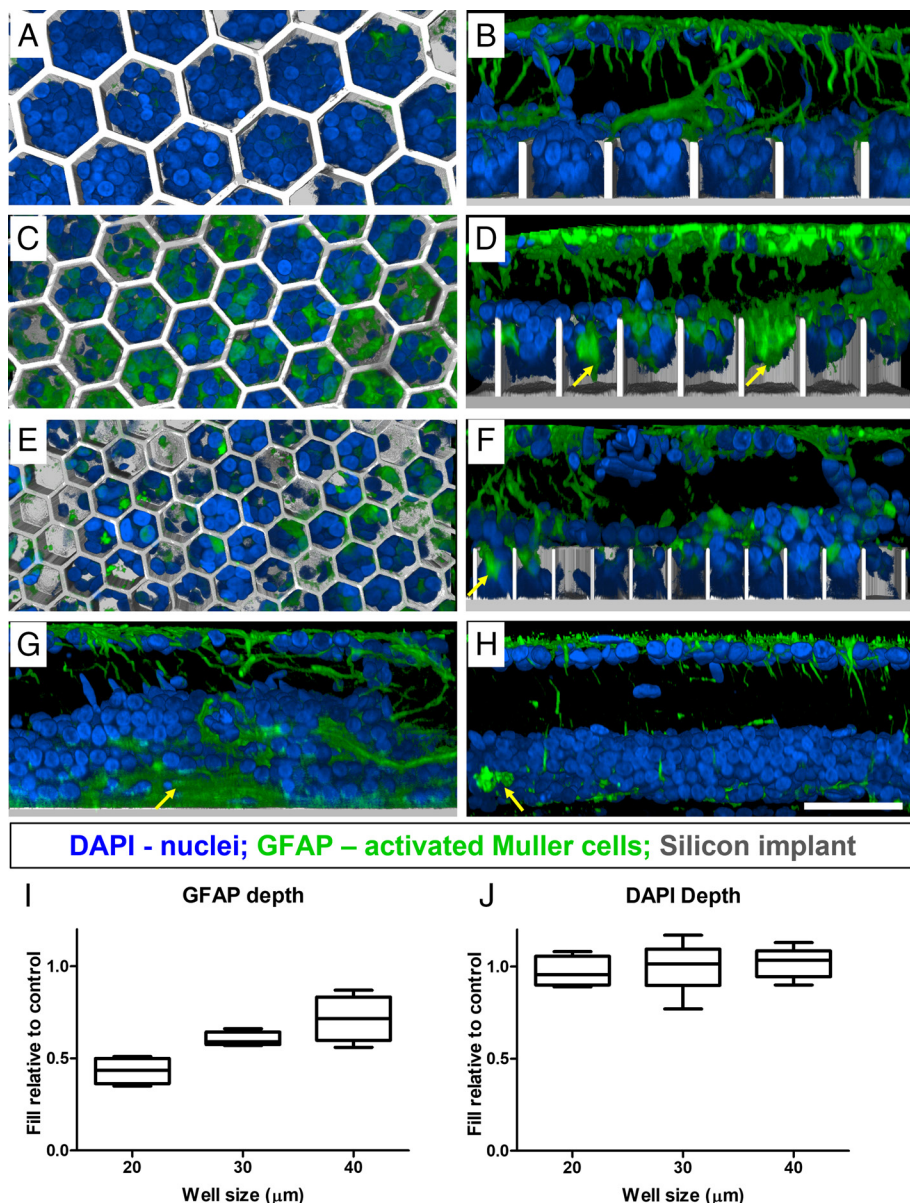


Fig. 7. Müller cell activation marker GFAP (green), DAPI (blue) label the nuclei, and the implant is shown in grey. (Scale bar is 50 μm .) Top-down view (left column) and side view (right column) show the retina above and inside honeycomb wells of 40 (A and B), 30 (C and D), and 20 (E and F) μm . Yellow arrows point at large clusters of GFAP lacking the nuclei inside the wells and also above the flat implant (G) and nonimplanted control (H). Penetration of GFAP into wells (I) compared to DAPI nuclei penetration (J). Box extends from 25th to 75th percentile from the median line and whiskers—from smallest to largest value.

previous reports of the AC migration toward the GCL during retinal degeneration (40). The height of the walls impacts the extent of migration, cell types exposed to high electric field, and cross-talk between the pixels. The 25- μm depth provided a compromise between keeping the ACs out of the wells, having enough BCs in the wells, while maintaining good oxygenation. Achieving high grating acuity confirmed the functionality of prosthetic vision under these conditions. However, the ultimate optimization of the wall height should be further explored specifically for the thickness of human retina.

Müller cell activation and migration are a hallmark of retinal injury. During sustained retinal insult, Müller cell nuclear migration toward the injury site is thought to contribute to formation of a glial scar (46, 47). In the degenerate retina, glial seal formation and progression are associated with the later stages of retinal remodeling (40). In the presence of a 3-D array, the migration may be due to the surgical insult to the retina or a response to the same mediators that drive the other cell types. The fact that some

neurons migrate deeper than the Müller cells nuclei and GFAP indicates that they are not impeded by the presence of a glial seal. While several mechanisms and drivers of retinal cell motility have been identified in the developing retina (33, 35, 36), migration mediators in the presence of our implants have not been characterized. If a BC-specific migration mediator can be identified, it could be leveraged to promote the BC migration, while other cell types might be halted.

The biological feasibility and compatibility of the honeycomb structures demonstrated in our study pave the way for decreasing the pixel size down to 20 μm , thus enabling much higher resolution than with 100- μm flat bipolar pixels used in the current clinical trials (13). Fabrication of the durable and active honeycomb devices, based on electroplating the conductive walls with return electrodes on top, is in progress. If successful in clinical trials, this technology may enable prosthetic vision with acuity exceeding 20/100, which would be very beneficial for many patients blinded by retinal degeneration.

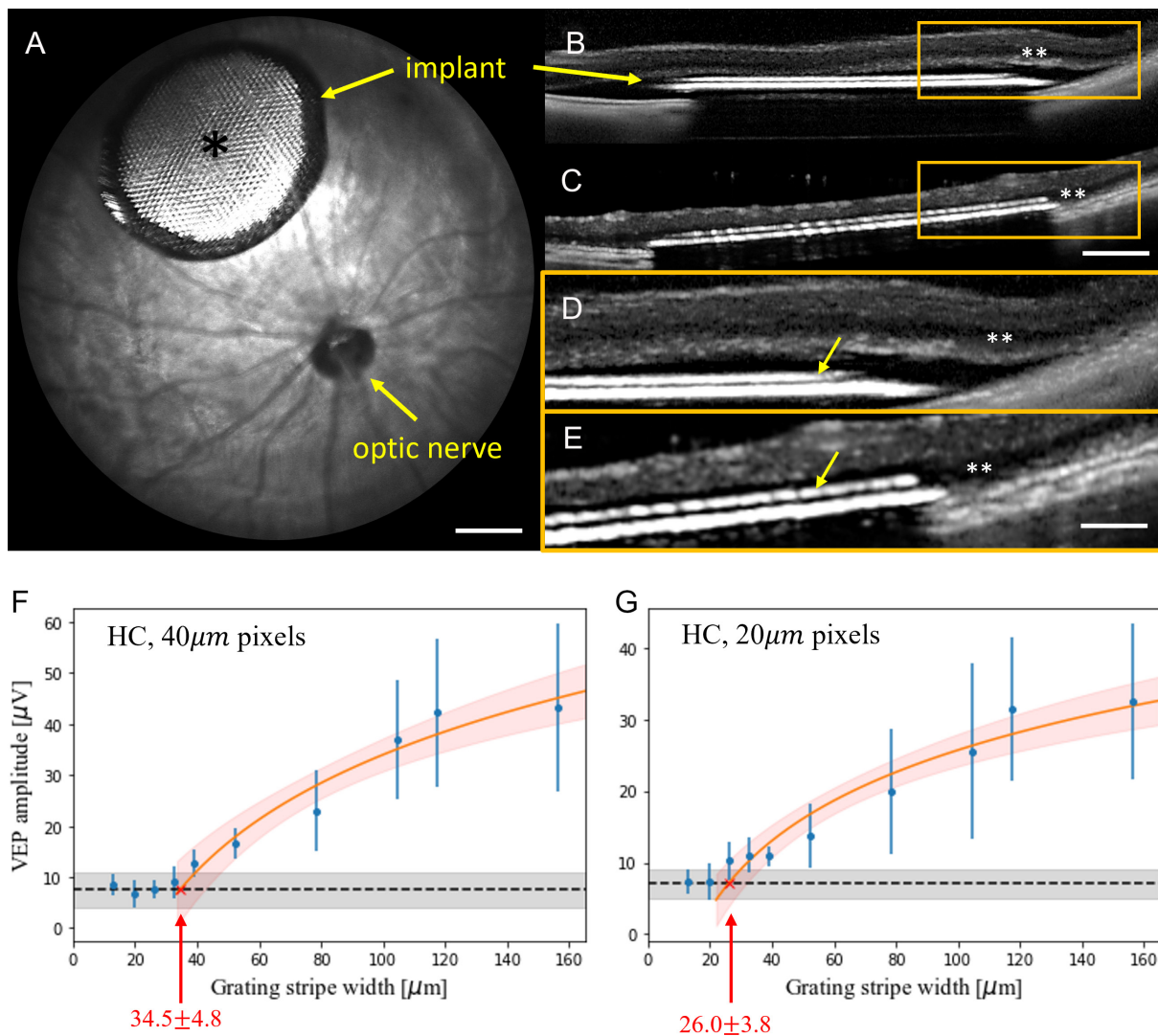


Fig. 8. (A) Fundus of a rat eye with a subretinal honeycomb implant. The light area (*) of the implant is the photovoltaic pixels with honeycomb walls, surrounded by the darker return electrode. (Scale bar is 500 μm .) (B) OCT image of the detached retina above the implant right after surgery and (C) 6 wk later. (Scale bar is 250 μm .) Migration of the INL (**) into the honeycomb wells (yellow arrows) can be observed by comparing the higher magnification OCT at day 0 (D) and week 6 (E). (Scale bar is 100 μm .) (F and G) VEP amplitude as a function of the grating bar width with honeycomb devices of (F) 40 μm and (G) 20 μm pixels. The error bars represent the SDs centered at mean values demonstrating variabilities among individual animals, which are derived from $n = 6$ (F) and $n = 5$ (G) biologically independent subjects. The black dashed lines represent the mean noise level, and the gray bands indicate the noise level range among animals. Red line is a logarithmic fit, which defines acuity as a crossing point with the noise level, pointed by the arrow. Red band around the fit line represents the 95% CI.

Methods

Honeycomb Implants. The INL in RCS rats is about 40 to 50 μm thick and is composed of 4 to 5 layers of nuclei. Assuming that AC nuclei are located in the top third of the INL, we made the walls 25 μm in height. Passive honeycomb implants for anatomical studies were fabricated from crystalline silicon using two mask layers to generate patterns for deep silicon etching, as previously described (15). Briefly, a hexamethyldisilazane primed wafer was spin-coated with 2 μm of negative photoresist (AZ5214-IR), which was then exposed to UV light through a patterned photomask. The 25- μm -deep cavities were then etched in the unprotected regions using a Bosch etch process. After the honeycomb-defining resist was removed, photoresist (7.5% SPR 220-7, 68% MEK, and 24.5% PGMEA) was spray-coated over the wafer to a thickness of 30 μm and exposed to define the releasing trenches around the 1-mm-wide arrays, also using a Bosch process. The wafer was then spray-coated with a protective 60- μm -thick photoresist for the backside grinding from 500 to 50 μm in thickness from the base of the honeycombs. Subsequent etching of the remaining excess silicon in XeF₂ gas completed the release of the implants. Each implant had four quadrants with hexagonal honeycomb patterns 40, 30, and 20 μm in width and having 25- μm -high walls of 4, 3, and 2 μm thicknesses, respectively. The fourth quadrant served as a flat

control, shown in Fig. 1 C and D. Arrays were sputter-coated with 200 nm of gold to prevent dissolution of the oxidized silicon (300 nm) in vivo.

For the studies of retinal stimulation, 25- μm tall polymer walls were made with two-photon lithography (Nanoscribe GmbH & Co. KG, Karlsruhe, Germany) atop monopolar photovoltaic arrays (28). These arrays are 1.5 mm in diameter, containing a 1.2-mm-wide hexagonal grid of either 821 pixels 40 μm in size, or 2,806 pixels of 20 μm . Each pixel has a vertical junction photodiode with the anode connected to a disk coated with SIROF as the active electrode, and the cathode connected to a large annulus SIROF electrode as the global return in the periphery of the array (28). The resulting active honeycomb implant with 40- μm pixels is shown in Fig. 1E. The 40- μm pixels included an active electrode of 16 mm diameter, pointed by the arrow in Fig. 1E, while in 20 μm pixels, the active electrode was 8 mm in diameter.

Animals and Surgical Procedures. All experimental procedures were approved by the Stanford Administrative Panel on Laboratory Animal Care and conducted in accordance with the institutional guidelines and conformed to the Statement for the Use of Animals in Ophthalmic and Vision research of the Association for Research in Vision and Ophthalmology (ARVO). Animal care and subsequent implantations were conducted as previously described (48) using rats with retinal

degeneration from a RCS colony maintained at the Stanford Animal Facility. Total of $N = 33$ animals were implanted with passive honeycomb arrays and $N = 10$ animals with active honeycomb arrays after age of P180 to ensure complete degeneration of the photoreceptors. Animals were anesthetized with a mixture of ketamine (75 mg/kg) and xylazine (5 mg/kg) injected intraperitoneally. A 1.5-mm incision was made through the sclera and choroid 1 mm posterior to the limbus. The retina was detached with an injection of saline solution, and the implant was inserted into the subretinal space at least 3 mm away from the incision site. The conjunctiva was sutured with nylon 10-0, and topical antibiotic (bacitracin/polymyxin B) was applied on the eye postoperatively. Surgical success and retinal reattachment were verified using OCT (HRA2-Spectralis; Heidelberg Engineering, Heidelberg, Germany).

Retinal Immunohistochemistry. For the retinal imaging and analysis, animals were euthanized 6 to 9 wk post implantation using an intracardiac injection of phenytoin/pentobarbital (Euthanasia Solution; VetOne, Boise, ID, USA). The eyes were enucleated and rinsed in phosphate-buffered saline (PBS), anterior segment and lens were removed, the eye cup was cut to a 3 × 3-mm square centered around the implant and fixed in 4% paraformaldehyde (EMS, PA, USA) for 12 h at 4 °C. Samples were permeabilized with 1% Triton X-100 (Sigma-Aldrich, CA, USA) in PBS for 3 h at room temperature, followed by a blocking step in 10% bovine serum albumin (BSA) for 1 h at room temperature, and a 48-h incubation at room temperature with primary antibodies (*SI Appendix, Table S1*) in 0.5% Triton X-100, 5% BSA in PBS. Samples were washed for 6 h at room temperature in 0.1% Tween-20 in PBS (PBS-T), incubated for 48 h at room temperature with secondary antibodies (*SI Appendix, Table S1*), and counterstained with DAPI in PBS. After 6 h of washing in PBS-T, the samples were mounted with Vectashield medium (H-1000; Vector Laboratories, Burlingame, CA, USA).

Whole-Mount Retinal Imaging and Analysis. 3-D imaging of the retinal whole mounts was performed using a Zeiss LSM 880 Confocal Inverted Microscope with Zeiss ZEN Black software. The implant surfaces were identified by reflection of a 514-nm laser with a neutral-density beam splitter allowing 80% transmission and 20% reflection. The images were acquired through the total thickness of the retina using a Z-stack, with the upper and lower bounds defined at the inner limiting membrane and 10 μm below the base of the honeycomb wells, respectively. Stacks were acquired in the center of each honeycomb quadrant using a 40× oil-immersion objective with acquisition area >225 × 225 μm and 380 to 470 nm z-steps. The Zeiss z-stack correction module was used to account for dimmer light within the wells of the implants.

Confocal fluorescence datasets were processed using the Fiji distribution of ImageJ (49). To correct for brightness variations at different Z positions in the stack within the wells and above the implant, we first maximized the contrast in the individual XY planes to ensure 0.3% channel saturation. The XY planes were despeckled with the median filter and the background was suppressed using the rolling-ball algorithm (50). The images then underwent cascades of gamma adjustments and min-max corrections to further suppress the background, depending on the noise level. Gaussian blurring was applied for nucleus staining channels to smoothen the brightness variations within individual cells. The implants were reconstructed by extruding the implant reflection toward the bottom (extraocular side) of the image stack.

To quantify the number of cells in the wells, the 3-D image of each honeycomb well was segmented into voxels based on the reflection channel using the Moore-Neighbor tracing algorithm implemented by the "bwboundaries" function in MATLAB 2021b (Mathworks, Inc., Natick, MA), while a control image stack (without an implant) was treated as one segment. Voxels brighter than 15% of the maximum intensity were considered positive, and in each segment, we defined three metrics as follows: 1) cell count—the manually counted total number of cell bodies or nuclei; 2) filling percentage—a fraction of positive voxels; 3) migration depth—the 95th percentile of the depths for all positive voxels, counting from the top of the segment.

Electrophysiology. For measurement of the VEP, each animal was implanted with three transcranial electrodes: one electrode above the visual cortex of each

hemisphere (4 mm lateral from midline, 6 mm caudal to bregma), and a reference electrode in the somatosensory cortex (2 mm right of midline and 2 mm anterior to bregma).

For the pattern projection, following anesthesia and pupil dilation, viscoelastic gel was put between the cornea and a cover slip to cancel the corneal optical power and ensure good retinal visibility. The subretinal implant was illuminated using a customized projection system, including a NIR laser at 880 nm wavelength (MF_880 nm_400 um, DILAS, Tucson, AZ), collimating optics, and a digital micromirror display (DLP Light Commander; LOGIC PD, Carlsbad, CA) for generating optical patterns. The entire optical system was integrated with a slit lamp (Zeiss SL-120; Carl Zeiss, Thornwood, NY) for convenience of observing the illuminated retina in real time via a CCD camera (acA1300-60gmNIR; Basler, Ahrensburg, Germany).

To measure the stimulation threshold, NIR stimuli were applied at 2 Hz, with a pulse duration of 10 ms and peak irradiance ranging from 0.002 to 4.7 mW/mm² on the retina. The light intensity was measured at the cornea and then scaled to the retinal irradiance by the ocular magnification squared, where the magnification was defined as the ratio between the sizes of the projected pattern on the retina and on the cornea. VEPs were recorded using the Espion E3 system (Diagnosys LLC, Lowell, MA) at a sampling rate of 2 kHz and averaged over 500 trials. The stimulation threshold was defined as the VEP amplitude exceeding the noise above the 95% CI, as described previously (28, 51).

For visual acuity assessment, irradiance of the NIR stimuli was fixed at 2.4 mW/mm², and alternating gratings were applied in 4-ms-long pulses, at a carrier frequency of 64 Hz and a grating switching cycle of 1 Hz (500 ms per image). The grating bar widths varied from 13 μm to 157 μm on the retina. The noise baseline for acuity measurements was determined by projecting static gratings of 120-μm bar width, with other stimulus parameters held identical to the alternating gratings experiments.

VEP data analysis was performed using a custom code developed in MATLAB and Python. High-frequency components in VEP waveforms responding to the pulsed stimuli were filtered out via a spectrum reconstruction algorithm. The visual acuity limit was estimated as the intersection of the logarithmic fit of data points above noise level with the noise band (representing 1 SD on each side), as previously described (51). The intersection between the VEP fit line and the mean noise level was defined as the nominal acuity limit, while the intersections between the fitted curve and the upper and lower bounds of noise band indicated uncertainties.

Data, Materials, and Software Availability. All study data are included in the article and/or *SI Appendix*.

ACKNOWLEDGMENTS. We would like to thank Ethan Rosenfeld from the Department of Physics at Stanford for his help with confocal image processing. M.B.B. performed surgeries, *in vivo* imaging, immunohistochemistry, and confocal imaging; M.B.B. and Z.C.C. conducted image processing and statistical analysis; M.B.B. and B.-Y.W. conducted the electrophysiological measurements; Z.C.C., A.S., T.H., and L.G. fabricated subretinal implants under the guidance of K.M. and T.K.; D.P. guided the research and data analysis; all authors participated in writing and/or reviewing the manuscript. Studies were supported by the NIH (Grants R01-EY-027786, and P30-EY-026877), the Department of Defense (Grant W81XWH-22-1-0933), Air Force Office of Scientific Research (Grant FA9550-19-1-0402), Wu Tsai Institute of Neurosciences at Stanford, and unrestricted grant from the Research to Prevent Blindness. Photovoltaic arrays were fabricated at the Stanford Nano Shared Facilities and Stanford Nanofabrication Facility, which are supported by the NSF award ECCS1542152. K.M. was supported by a Royal Academy of Engineering Chair in Emerging Technology, UK.

Author affiliations: ^aHansen Experimental Physics Laboratory, Stanford University, Stanford, CA 94305; ^bDepartment of Ophthalmology, Stanford University, Stanford, CA 94305; ^cDepartment of Physics, Stanford University, Stanford, CA 94305; ^dDepartment of Electrical Engineering, Stanford University, Stanford, CA 94305; ^eDepartment of Material Science, Stanford University, Stanford, CA 94305; and ^fDepartment of Physics, University of Strathclyde, G1 1XQ Glasgow, Scotland, United Kingdom

1. J. L. Stone, W. E. Barlow, M. S. Humayun, E. de Juan, A. H. Milam, Morphometric analysis of macular photoreceptors and ganglion cells in retinas with retinitis pigmentosa. *Arch. Ophthalmol. Chic. Ill* **1960**, 1634–1639 (1992).
2. S. Y. Kim *et al.*, Morphometric analysis of the macula in eyes with geographic atrophy due to age-related macular degeneration. *Retina Phila. Pa* **22**, 464–470 (2002), 10.1097/00006982-20020800-00011.
3. M. S. Humayun *et al.*, Morphometric analysis of the extramacular retina from postmortem eyes with retinitis pigmentosa. *Invest. Ophthalmol. Vis. Sci.* **40**, 143–148 (1999).
4. B. W. Jones *et al.*, Retinal remodeling and metabolic alterations in human AMD. *Front. Cell. Neurosci.* **10**, 103 (2016), 10.3389/fncel.2016.00103.
5. C. Sekirnjak *et al.*, Changes in physiological properties of rat ganglion cells during retinal degeneration. *J. Neurophysiol.* **105**, 2560–2571 (2011), 10.1152/jn.01061.2010.
6. L. da Cruz *et al.*, Five-year safety and performance results from the Argus II retinal prosthesis system clinical trial. *Ophthalmology* **123**, 2248–2254 (2016), 10.1016/j.ophtha.2016.06.049.
7. T. L. Edwards *et al.*, Assessment of the electronic retinal implant alpha AMS in restoring vision to blind patients with end-stage retinitis pigmentosa. *Ophthalmology* **125**, 432–443 (2018), 10.1016/j.ophtha.2017.09.019.
8. J. Cehajic Kapetanovic *et al.*, Highest reported visual acuity after electronic retinal implantation. *Acta Ophthalmol. (Copenh.)* **98**, 736–740 (2020), 10.1111/aos.14443.
9. H. Lorach *et al.*, Photovoltaic restoration of sight with high visual acuity. *Nat. Med.* **21**, 476–482 (2015), 10.1038/nm.3851.
10. K. Mathieson *et al.*, Photovoltaic retinal prosthesis with high pixel density. *Nat. Photonics* **6**, 391–397 (2012), 10.1038/nphoton.2012.104.
11. E. Ho *et al.*, Spatiotemporal characteristics of retinal response to network-mediated photovoltaic stimulation. *J. Neurophysiol.* **119**, 389–400 (2018), 10.1152/jn.00872.2016.
12. D. Palanker, Y. Le Mer, S. Mohand-Said, M. M. K. Muqit, J. A. Sahel, Photovoltaic restoration of central vision in atrophic age-related macular degeneration. *Ophthalmology* **127**, 1097–1104 (2020), 10.1016/j.ophtha.2020.02.024.
13. D. Palanker, Y. Le Mer, S. Mohand-Said, J. A. Sahel, Simultaneous perception of prosthetic and natural vision in AMD patients. *Nat. Commun.* **13**, 513 (2022), 10.1038/s41467-022-28125-x.
14. J. D. Loudin *et al.*, Optoelectronic retinal prosthesis: System design and performance. *J. Neural Eng.* **4**, S72–S84 (2007), 10.1088/1741-2560/4/1/S09.
15. T. Flores *et al.*, Honeycomb-shaped electro-neural interface enables cellular-scale pixels in subretinal prosthesis. *Sci. Rep.* **9**, 1–12 (2019), 10.1038/s41598-019-47082-y.
16. B.-Y. Wang, Z. C. Chen, M. Bhuckor, A. K. Goldstein, D. Palanker, Pixel size limit of the PRIMA implants: From humans to rodents and back. *J. Neural. Eng.* **19**, 055003 (2022), 10.1088/1741-2552/ac8e31.
17. E. Ho *et al.*, Characteristics of prosthetic vision in rats with subretinal flat and pillar electrode arrays. *J. Neural. Eng.* **16**, 066027 (2019), 10.1088/1741-2552/ab34b3.
18. M. Djilas *et al.*, Three-dimensional electrode arrays for retinal prostheses: Modeling, geometry optimization and experimental validation. *J. Neural Eng.* **8**, 046020 (2011), 10.1088/1741-2560/8/4/046020.
19. A. Butterwick *et al.*, Effect of shape and coating of a subretinal prosthesis on its integration with the retina. *Exp. Eye Res.* **88**, 22–29 (2009), 10.1016/j.exer.2008.09.018.
20. D. Palanker *et al.*, Migration of retinal cells through a perforated membrane: Implications for a high-resolution prosthesis. *Invest. Ophthalmol. Vis. Sci.* **45**, 3266–3270 (2004), 10.1167/iovs.03-1327.
21. P. G. Losada *et al.*, Protruberant electrode structures for subretinal electrical stimulation: Modeling, fabrication and in vivo evaluation. *Front. Neurosci.* **13**, 885 (2019), <https://www.frontiersin.org/articles/10.3389/fnins.2019.00885>.
22. Y. Chu, M. F. Humphrey, I. J. Constable, Horizontal cells of the normal and dystrophic rat retina: A wholemount study using immunolabelling for the 28-kDa calcium-binding protein. *Exp. Eye Res.* **57**, 141–148 (1993), 10.1006/exer.1993.1109.
23. H. Kolb, "Roles of amacrine cells" in *Webvision: The Organization of the Retina and Visual System*, H. Kolb, E. Fernandez, R. Nelson, Eds. (University of Utah Health Sciences Center, Salt Lake City (UT), 2007), <http://www.ncbi.nlm.nih.gov/books/NBK11539/>.
24. J. P. Campbell *et al.*, Detailed vascular anatomy of the human retina by projection-resolved optical coherence tomography angiography. *Sci. Rep.* **7**, 42201 (2017), 10.1038/srep42201.
25. G. P. Lewis, E. A. Chapin, G. Luna, K. A. Linberg, S. K. Fisher, The fate of Müller's glia following experimental retinal detachment: nuclear migration, cell division, and subretinal glial scar formation. *Mol. Vis.* **16**, 1361–1372 (2010).
26. G. P. Lewis, S. K. Fisher, Up-regulation of glial fibrillary acidic protein in response to retinal injury: Its potential role in glial remodeling and a comparison to vimentin expression. *Int. Rev. Cytol.* **230**, 263–290 (2003).
27. D. Goldman, Müller glial cell reprogramming and retina regeneration. *Nat. Rev. Neurosci.* **15**, 431–442 (2014), 10.1038/nrn3723.
28. T. W. Huang *et al.*, Vertical-junction photodiodes for smaller pixels in retinal prostheses. *J. Neural Eng.* **18**, 036015 (2021), 10.1088/1741-2552/abe668.
29. D. C. Lozano, M. D. Twa, Development of a rat schematic eye from *in vivo* biometry and the correction of lateral magnification in SD-OCT imaging. *Invest. Ophthalmol. Vis. Sci.* **54**, 6446–6455 (2013), 10.1167/iovs.13-12575.
30. L. C. Silveira, C. A. Heywood, A. Cowey, Contrast sensitivity and visual acuity of the pigmented rat determined electrophysiologically. *Vision Res.* **27**, 1719–1731 (1987), 10.1016/0042-6989(87)90101-5.
31. P. Seymour, J. M. Juraska, Vernier and grating acuity in adult hooded rats: The influence of sex. *Behav. Neurosci.* **111**, 792–800 (1997), 10.1037/0735-7044.111.4.792.
32. G. T. Prusky, P. W. West, R. M. Douglas, Behavioral assessment of visual acuity in mice and rats. *Vision Res.* **40**, 2201–2209 (2000), 10.1016/s0042-6989(00)00081-x.
33. M. Rocha-Martins *et al.*, Neuronal migration prevents spatial competition in retinal morphogenesis. *Nature* **620**, 615–624 (2023), <https://doi.org/10.1038/s41586-023-06392-y>.
34. G. B. Colin *et al.*, Disruption in murine Em1 perturbs retinal lamination during early development. *Sci. Rep.* **10**, 5647 (2020), 10.1038/s41598-020-62373-5.
35. R. Amini *et al.*, Amoeboid-like migration ensures correct horizontal cell layer formation in the developing vertebrate retina. *eLife* **11**, e76408 (2022), 10.7554/elife.76408.
36. R. Amini, M. Rocha-Martins, C. Norden, Neuronal migration and lamination in the vertebrate retina. *Front. Neurosci.* **11**, 742 (2018), 10.3389/fnins.2017.00742.
37. L. M. Baye, B. A. Link, Nuclear migration during retinal development. *Brain Res.* **1192**, 29–36 (2008), 10.1016/j.brainres.2007.05.021.
38. J. Ichai, C. Kunath, M. Rocha-Martins, C. Norden, Independent modes of ganglion cell translocation ensure correct lamination of the zebrafish retina. *J. Cell Biol.* **215**, 259–275 (2016), 10.1083/jcb.201604095.
39. E. Strettoi, V. Pignatelli, C. Rossi, V. Porciatti, B. Falsini, Remodeling of second-order neurons in the retina of rd/rd mutant mice. *Vision Res.* **43**, 867–877 (2003), 10.1016/s0042-6989(02)00594-1.
40. R. Sullivan, P. Penfold, D. V. Pow, Neuronal migration and glial remodeling in degenerating retinas of aged rats and in nonneovascular AMD. *Invest. Ophthalmol. Vis. Sci.* **44**, 856–865 (2003).
41. R. E. Marc, B. W. Jones, C. B. Watt, E. Strettoi, Neural remodeling in retinal degeneration. *Prog. Retin. Eye Res.* **22**, 607–655 (2003), 10.1016/s1350-9462(03)00039-9.
42. S. K. Fisher, G. P. Lewis, K. A. Linberg, M. R. Verardo, Cellular remodeling in mammalian retina: results from studies of experimental retinal detachment. *Prog. Retin. Eye Res.* **24**, 395–431 (2005), 10.1016/j.preteyer.2004.10.004.
43. Y. M. Paulus *et al.*, Healing of retinal photoocoagulation lesions. *Invest. Ophthalmol. Vis. Sci.* **49**, 5540–5545 (2008), 10.1167/iovs.08-1928.
44. R. E. Marc *et al.*, Extreme retinal remodeling triggered by light damage: Implications for age related macular degeneration. *Mol. Vis.* **14**, 782–805 (2008).
45. C. Blazynski, Displaced cholinergic, GABAergic amacrine cells in the rabbit retina also contain adenosine. *Vis. Neurosci.* **3**, 425–431 (1989).
46. J. Sugita *et al.*, The role of interleukin-33 expression in retinal tissue. *Invest. Ophthalmol. Vis. Sci.* **55**, 708–708 (2014).
47. H. Xi *et al.*, IL-33 amplifies an innate immune response in the degenerating retina. *J. Exp. Med.* **213**, 189–207 (2016), 10.1084/jem.20150894.
48. H. Lorach *et al.*, Performance of photovoltaic arrays in-vivo and characteristics of prosthetic vision in animals with retinal degeneration. *Vision Res.* **111**, 142–148 (2015), 10.1016/j.visres.2014.09.007.
49. J. Schindelin *et al.*, Fiji: An open-source platform for biological-image analysis. *Nat. Methods* **9**, 676–682 (2012), 10.1038/nmeth.2019.
50. A. J. Hanson, "The rolling ball" in *Graphics Gems III*, D. Kirk, Ed. (Academic Press Professional Inc, USA, 1992), pp. 51–60.
51. B.-Y. Wang *et al.*, Electronic photoreceptors enable prosthetic visual acuity matching the natural resolution in rats. *Nat. Commun.* **13**, 6627 (2022), 10.1038/s41467-022-34353-y.